

# Lawrence Berkeley National Laboratory

## Lawrence Berkeley National Laboratory

### **Title**

Using aberration test patterns to optimize the performance of EUV aerial imaging microscopes

### **Permalink**

<https://escholarship.org/uc/item/1q32n86p>

### **Author**

Mochi, Iacopo

### **Publication Date**

2009-09-15

Peer reviewed

# Using aberration test patterns to optimize the performance of EUV aerial imaging microscopes

Iacopo Mochi, Kenneth A. Goldberg, Ryan Miyakawa, Patrick Naulleau  
CXRO, Lawrence Berkeley National Laboratory, Berkeley, CA 94720 , USA

Hak-Seung Han

Photomask Team, SAMSUNG ELECTRONICS Co., LTD, Korea

Sungmin Huh

SEMATECH, 255 Fuller Road, Suite 309, Albany, NY 12203, USA

The SEMATECH Berkeley Actinic Inspection Tool (AIT) is a prototype EUV-wavelength zoneplate microscope that provides high quality aerial image measurements of EUV reticles. To simplify and improve the alignment procedure we have created and tested arrays of aberration-sensitive patterns on EUV reticles and we have compared their images collected with the AIT to the expected shapes obtained by simulating the theoretical wavefront of the system. We obtained a consistent measure of coma and astigmatism in the center of the field of view using two different patterns, revealing a misalignment condition in the optics.

## I. Introduction

The SEMATECH Berkeley Actinic Inspection Tool (AIT) is a prototype EUV-wavelength zoneplate microscope that provides high quality aerial image measurements of EUV reticles [1]. To achieve the highest possible imaging performance, in terms of contrast, resolution, and measurement repeatability, optical alignment must be maintained. This is especially important in the AIT because the aberration-corrected “sweet spot” of the field of view is relatively small, approximately 5–8- $\mu\text{m}$  diameter.

---

A single AIT image records visible area 30- $\mu\text{m}$  wide; the variation of the imaging performance, and the degradation away from the sweet spot is readily apparent. In the AIT, it is possible to select one of five available objective lenses with different numerical aperture and magnification values. While switching between lenses in the AIT is easy (requiring less than two minutes), achieving the highest imaging performance is a complex task and requires a quick and reliable alignment optimization procedure.

The first step to optimize the alignment of an optical system is to model and quantify its aberrations within the field of view and to understand the aberration dependencies on the available degrees of freedom. Ray-tracing modeling provides a predictive map of the field of view, as it would appear in an ideal system, and reveals how the aberrations vary when the alignment parameters are changed. With that in mind an effective strategy for minimizing the aberrations of the system is to compare the measured aberrations with simulations and utilize the alignment parameters that have the strongest effect on the aberrations. In the AIT, the illumination angle and the zoneplate position are the most sensitive alignment parameters. The illumination angle affects the intensity variation, while the zoneplate position affects the optical aberrations and their variation across the field.

Previously, we have reported the use of *contact arrays*, which are patterns of dense or isolated point-like image features, as aberration monitors [2]. Through-focus analysis of the contact arrays provides a highly sensitive astigmatism monitor when other aberrations are small. In the presence of large aberrations, when the Strehl ratio is reduced, the point-like features can become difficult to measure and interpret accurately: the dynamic range of this technique may be limited.

---

To improve the alignment procedures we have created and tested arrays of more complex aberration-sensitive patterns on EUV reticles. Other groups have discussed aberration -probe patterns that utilize phase-shifting patterns with feature sizes approaching the resolution of the optical systems under test, [4]. Here, we consider binary patterns with feature sizes that are somewhat larger than the resolution. In part this self-imposed restriction is done by necessity, owing to the limitations of available EUV mask and pattern fabrication. We will discuss the technique we used to match the measured through-focus test pattern images with model data to achieve quantitative aberration measurement to improve the AIT alignment.

## II. Raytracing simulation

The AIT has a rather simple optical system [1]. The only element with optical power is a single off-axis zoneplate lens that forms a highly magnified image of the reticle surface on a EUV sensitive camera (figure 1). The AIT has up to five user-selectable zoneplates with different numerical aperture (NA) and magnification values; the zoneplate used in this analysis has a NA of 0.0875 (emulating the spatial resolution of a 4x, 0.35-NA stepper), a focal length of 750  $\mu\text{m}$  and a working angle of 6 degrees. The zoneplate was fabricated with electron-beam lithography as a gold pattern on a 100-nm-thick silicon-nitride membrane, with a diameter of 131  $\mu\text{m}$ .

In principle, an optical system made with an ideal single lens can be aberration -free in just one point, along the optical axis; the other points of the field of view are affected by some amount of aberration. In an area close to the optical axis, aberrations are small enough that the performance may be described as *diffraction limited*, where the aberrations have negligible effect on image quality. The AIT is an off-axis system, with a tilted field of view; there is a linearly

---

varying defocus error in the off-axis displacement direction that reduces the single-image sweet spot size.

To evaluate the size of this area we calculated the RMS wavefront error and the Strehl ratio for the AIT in the perfect alignment configuration. If we consider as negligible aberrations creating an RMS wavefront error smaller than  $\lambda/20$ , then the sweet spot of the AIT has a width of  $8 \mu\text{m}$  and a height of  $5 \mu\text{m}$ . If we restrict the sweet spot definition to those points with a predicted Strehl ratio greater than 95%, the area is  $5.5 \mu\text{m}$  wide and  $3.5 \mu\text{m}$  tall (figure 2). The elliptical appearance of this sweet spot is due to a spatially varying defocus component that is characteristic of off-axis single-lens systems. In the majority of the cases we study, it is possible to acquire a through-focus image series and identify the image where the defocus term is locally minimized. Figure 3 shows the enlarged shape of the sweet spot through focus, obtained by removing the defocus term from the wavefront error.

If the system is perfectly aligned, the sweet spot is located in the middle of the field of view, but a  $10\text{-}\mu\text{m}$  displacement of the zoneplate lens degrades the image quality beyond its useful range. As a first approximation, if the lens is misplaced of  $15 \mu\text{m}$ , the sweet spot will fall outside the field of view and the image resolution will be limited by the aberrations everywhere.

We utilize the aberration variation across the field of view to assess the alignment status of the system. We used *Zemax* to calculate the spatial distribution of the main aberrations that affect the AIT, sampling the field at an array of  $21 \times 21$  positions [2] or more. This analysis shows the focal plane's tilt and reveals that the most significant aberrations are astigmatism and, to a lesser degree, coma, as expected for an off-axis system (see table 1). Spherical aberration and other higher order aberration terms give a negligible contribution to the wavefront error, with a maximum combined contribution of  $0.003$  waves RMS.

When the system is misaligned, the distribution of these aberrations in the field of view changes and the comparison between the predicted and measured aberration map provides shows us how to correct the alignment through the adjustment of the available freedom degrees [2].

### **III. Patterns description**

We designed and tested various patterns to reveal and quantify the presence of astigmatism and coma. Each pattern, shown in Fig. 4, is constituted by a single, small glyph, rotated into more than one orientation, and replicated over an area of  $5050 \mu\text{m}$ , greater than the AIT's single -image viewable area. This allowed us to cover in one image the AIT's whole field of view. We scaled the glyph sizes to create patterns above the nominal resolution limit of the AIT, which, for the zoneplate we are considering in this analysis, is  $93 \text{ nm}$ . The shape of these glyphs were designed keeping in mind two assumptions: parallel lines close together tend to blur and bridge at specific focal planes that depend on their direction with respect to the astigmatism's axes and single dots and isolated lines show an asymmetric blurring in presence of coma.

The two simplest patterns are arrays of  $120 \text{ nm}$  square contacts: one dense array (Fig. 4-E) with spacing of  $120 \text{ nm}$ , and a sparse array (Fig. 4-F) where the spacing between the squares is  $480 \text{ nm}$ .

The other glyphs that constitute the test patterns are a square frame of  $360 \text{ nm}$  side and  $120 \text{ nm}$  thickness (figure 4-A); a square frame with  $600 \text{ nm}$  side,  $120 \text{ nm}$  thickness and a  $120 \text{ nm}$  square contact nested in the middle (figure 4-B), and a symbol made with horizontal and vertical features arranged to be symmetric with respect to a  $45$  degrees axis only (figure 4-C). Each pattern was created alternating one glyph and its copy rotated of  $45$  degrees.

---

One additional test pattern features an array of five densely spaced lines, 1080 nm long and 120 nm thick and with 120 nm spacing, in four orientations corresponding to 0, 45, 90, and 135 degrees (figure 4-D). This pattern shares the important properties of nested elbow patterns, which are commonly used to manually measure the local astigmatic displacement.

These aberration test patterns were included on a EUV test mask provided by Samsung. The complete array of aberration patterns has an area of about 1 00150  $\mu\text{m}^2$  and fits easily among the other test features on the mask.

#### ***IV. Aberration measurement***

There are many ways to extract aberration measurements from the behavior of patterns through focus. Here we describe two methods we have used that are well suited to measuring astigmatism, our most significant aberration. We also present an additional method based on a direct pattern-matching algorithm relying on a genetic optimization routine.

##### ***A. Lines in four orientations.***

A coarse measurement of the local astigmatism, expressed as a combination of Zernike polynomials, can be made from a through-focus image series of pattern D. To measure the local components of astigmatism each measurement point must contain enough focal range to reach the sagittal and tangential focal planes. With pattern D, the astigmatic displacement can be estimated from a visual inspection of the images, knowing the displacement between the sagittal and tangential foci. The relation between the astigmatic displacement  $AD$  (measured in the image space) and the astigmatism FRINGE coefficient  $S$  is given by :

---

where  $a$  is the radius of the exit pupil and  $R$  is the radius of the converging wavefront on the object side. Approximating the numerical aperture as the ratio between  $a$  and the focal length of the system, we can rearrange equation 1 as:

$$S = \frac{AD}{2} NA^2 \quad (2)$$

where  $AD'$  is the astigmatic displacement measured in the object space. The astigmatic displacement between horizontal and vertical lines provides the value of the  $0^\circ$  astigmatism coefficient while the  $45^\circ$  astigmatism coefficient is obtained from the  $AD$  measured with two sets of oblique lines. The sensitivity of this method is limited by the longitudinal, focal step size between images. In the case of the AIT, the minimum step size in a through-focus series is typically  $0.4 \mu\text{m}$ , which means that the smallest amount of astigmatism detectable is approximately 0.1 waves.

Compared with other patterns, the relatively large size of the repeated line pattern limits the density of aberration measurement points that are available to us within a single field.

**B. Contact-field measurement.** With contact patterns, the local astigmatic displacement can be determined accurately by

measuring the evolution of the elliptical blurring through-focus. Previously, we reported the use of this technique with an array of 175-nm square contacts [2]. We were able to calculate the local astigmatism to 0.001 waves (RMS). The contact fields may also be useful for the measurement of additional aberration terms. However, the low intensity of these isolated features out of focus and in the presence of large aberrations, likely degrades the signal to noise ratio of the images and the analysis.

**C. Generalized aberration extraction using a genetic algorithm and binary image patterns**

We have investigated the possibility of retrieving the magnitudes of aberration terms beyond astigmatism from the direct analysis of binary images with complex shapes. Using



through focus image series of different test patterns, we searched for the wavefront error that most closely reproduced the images collected with the AIT. We performed this search by simulating pattern images created by the AIT, under the influence of various trial wavefront errors. The simulated images are mathematically compared to the measured one using a simple merit function. The fitting parameters are the Zernike coefficients that describe the wavefront error. By optimizing the merit function we obtain the best estimate for all the component aberration terms.

This technique, with numerous variations, has been used with point-like objects centered in the field of view of the system under test, . Here we use the spatial variation of the aberrations across the visible field to understand and correct the optical system's misalignment, and to verify the location of the sweet spot. In principle, the measurement of a single object should provide enough information to reconstruct the wavefront [9]; nevertheless, the differing responses of the merit function reveal that each pattern has a specific sensitivity to different aberrations in different focal planes. On their own, individual images can produce ambiguous results. To overcome this problem and develop a more robust fitting procedure, we analyze series of images recorded through focus. We assume that within a series, defocus varies in a known way, and the other aberrations remain constant. This assumption provides redundancy that helps convergence and eliminates the ambiguity present in isolated images.

The parameter space we search depends on the number of Zernike polynomial terms that we want to take into account. Since the optical model showed that the main aberrations affecting the AIT are coma and astigmatism, we limited our search to the first seven polynomials, excluding the constant, piston term that doesn't affect the image shape. This restriction could be removed in future studies, and for the evaluation of arbitrary optical systems. The AIT raytracing

model was also used to predict the expected magnitude of the aberrations and to obtain a first guess of the parameters of the fit.

The merit function we used to perform the fit is simply the square difference of the real image and expected shape of the pattern in presence of a known wavefront. Let  $v$  be an  $(mn)$  array containing the collected image and  $b$  an array of the same size that we generated using the pattern shape and the wavefront error  $w$ . The merit function is given by the sum of the point-by-point square difference within the sub-image:

$$M(w) = \sum_{i,j} (v_{i,j} - u_{i,j}(w))^2 \quad (3)$$

The value of  $M$  is calculated after normalizing both  $v$  and  $u$  to their integral value to account for flux changes throughout the series and illumination variations across the field of view. The wavefront  $w$  is expressed as a linear combination of Zernike FRINGE polynomials. To find the aberrations affecting the collected image we minimized  $M$  with respect to the polynomials coefficients.

When the parameter space contains several free parameters (the Zernike polynomial coefficients), and the merit function is highly nonlinear, the potential for encountering local minima increases and makes the selection of a strong search algorithm necessary. We tested several fitting techniques, including least squares, direct search, and genetic algorithms [10]. Our experience showed that a genetic algorithm coupled with a least square fitting routine could be applied efficiently. The selection of an appropriate search algorithm could be a topic of lengthy investigations, beyond the scope of this article. Our method applies the genetic algorithm iteratively, and after each step probes for a global minimum using least squares.

## ***V. Pattern sensitivity to aberrations***

We explored the sensitivity of this technique, simulating the through-focus imaging and aberration estimation using different patterns and randomly selected wavefront error. For each pattern, we measured the method's sensitivity to astigmatism and coma (the main aberration in the AIT), calculating  $M$  for a range of aberration coefficient values, through focus. As expected, the sensitivity depends on the pattern shape, the type of aberration, and the focal position. For example, as shown in Fig. 5, if we restrict our analysis to one single aberration component, coma is more evident when the pattern is in focus, while astigmatism has a stronger effect on both sides of the best focal plane. Figure 5 shows the variation of the merit function  $M$  as a function of defocus for different patterns when the wavefront error has 0.2 waves RMS of 0<sup>o</sup> astigmatism (Z4) and 0.05 waves RMS of X coma (Z6), respectively. In both cases the merit function is calculated by comparing one image with increasing values of defocus and the same image where we have added either astigmatism or coma. We chose the aberration magnitude to match the maximum value that occurs within the field of view of the AIT when it is perfectly aligned (Table 1). For each pattern we studied a square sub-image containing four glyphs: two glyphs are required for sensitivity to both components of astigmatism and coma, the additional two improve the signal-to-noise ratio. We approximate the local aberrations as being constant within the sub-image. This approximation sets a single-point sensitivity limit for this technique that depends on the glyph array spacing. The raytracing calculation shows that, when the system is aligned, the maximum value of the RMS wavefront error gradient is 0.025 waves/ $\mu\text{m}$ . (This value occurs at the edges of the field). The four glyphs for patterns A, B, C, and D have spacings of 0.96, 1.20, 1.32 and 1.56  $\mu\text{m}$  respectively. This implies a single-point RMS sensitivity limit of 0.024 waves for pattern A, 0.030 waves for pattern B, 0.033 waves for pattern C and 0.039 waves for pattern D. While this effect raises the uncertainty in each point, the combined measurement of several different

field positions allows to obtain an aberration map that will provide a much more accurate feedback for the system alignment.

## IV. AIT data analysis

The method was applied to the analysis of imaging data collected in the AIT. The dataset presented here includes one series of through-focus images for pattern B and C. We selected a region containing four glyphs with different orientations (Fig. 6), located at an arbitrary point near the center of the field of view . The genetic algorithm was used to find the best-fit values of the tilt, defocus, astigmatism and coma Zernike coefficients for each image in the through focus series. A demonstration of this reconstruction is shown in figure 6. We assume that aside from defocus, each image in the series has the same astigmatism and coma.

When the glyph sub-images are extracted from the original CCD images, small misalignments in the glyph position can appear as wavefront tilt differences. In this way, the tilt components of the reconstructed wavefront only indicate image-registration differences within the series.

To test the method on real images collected with the AIT we had to overcome the problem of the apparent tilt variation from an image to the other. The AIT's off-axis configuration causes points in the field to move in a predictable way, through focus, giving the impression of a tilt effect. As a result, the tilt terms of the wavefront are inconsistent from image to image. While it may be possible to utilize the image centroid to correct positions (tilt) differences among the series images, we chose to leave the tilt coefficients as free parameters in the fit, knowing that they do not influence the wavefront aberrations we are interested in.

We performed the fitting for each image in the through focus series and we calculated the mean value for each aberration coefficient and its standard deviation. Figure 7 shows the results obtained testing the same field point of the AIT with pattern C and pattern B in the same alignment condition.

To evaluate the position of the sweet spot and improve the system alignment it is necessary to repeat this analysis at several positions across the field of view , and then reconstruct the aberration's spatial distribution.

## V. Conclusions

The goal of this work was to evaluate local wavefront aberrations based on through-focus image data. We designed several different patterns, and tested their sensitivity to aberrations typically observed in the field of view of the AIT. A raytracing model shows that the main aberrations affecting the AIT are astigmatism and coma. We sought to design pattern features in different orientations that would be easy to fabricate, and would exhibit sensitivity to the orthogonal components of the two aberrations.

The evaluation of wavefront aberration is done minimizing the difference between a real image and a simulated image of the pattern affected with known aberrations. Since this problem is sensitive to the presence of local minima in the merit function, we used a robust genetic algorithm coupled with a least square fitting routine to optimize the Zernike polynomial coefficients of the local wavefront error. The AIT raytracing model helped to define a starting point for the optimization algorithm and to constrain the parameters space to reasonable wavefront error magnitudes (within  $\pm 0.4$  waves RMS).

We tested this technique on aerial images of aberration test patterns, collected using a Samsung EUV test mask. The uncertainty magnitudes, up to 0.2 waves, are due in part to the intrinsic noise of the images, caused by the low reflectivity of the mask, in part to the poor alignment condition that affect the gradient of the aberrations across the field of view and, possibly, to imperfections in the printed pattern. Nonetheless the results obtained with the two different patterns are consistent and show the presence of a 0.3 waves RMS of coma, indicating that the system is not in a good alignment condition.

Now that the reconstruction algorithm has been demonstrated, future work will include the analysis of aberrations across the field of view for use in the alignment optimization of the AIT. Since the aberrations are slowly varying across the field, there may be an opportunity to provide the fitting method with additional *a priori* information to speed the calculation. We can also use the simulation methods to investigate new patterns that improve the sensitivity of this technique.

## Acknowledgments

The authors gratefully acknowledge the support of SEMATECH and many LBNL team members who make this research possible. The AIT's technical support team includes Nathan

Smith, Charles D. Kemp, Paul Denham, Robert Gunion, Brian Hoef, Hanjing Han, Kenneth Woolfe, Jeffrey Gamsby, and Ron Tackaberry. The AIT's chief engineer is Senajith Rekawa. Contributing scientists include Erik Anderson and James Macdougall. This work is funded by SEMATECH under Project LITH-343S2, and was performed under the auspices of the U.S. Department of Energy by University of California Lawrence Berkeley National Laboratory. This work was supported by the Director, Office of Science, of the U.S. Department of Energy under Contract No. DE-AC02-05CH11231.

- [1] K. A. Goldberg, I. Mochi, P. P. Naulleau, H. Han, and S. Huh, "Benchmarking EUV mask inspection beyond 0.25 NA." SPIE, 7122, 71222E (2008).
- [2] I. Mochi, K. A. Goldberg, P. Naulleau, and S. Huh, "Improving the performance of the actinic inspection tool with an optimized alignment procedure", SPIE 7271, 727123 (2009).
- [3] G. Robins, K. Adam, and A. Neureuther "Measuring optical image aberrations with pattern and probe based targets", J. Vac. Sci. Technol. B 20, 338 (2002).
- [4] J. Rubinstein and A. Neureuther "Through-focus pattern matching applied to double patterning", Proc. SPIE 7274, 72741A (2009).
- [5] P. P. Naulleau, J. P. Cain, and K. A. Goldberg, "Lithographic characterization of the field dependent astigmatism and alignment stability of a 0.3 numerical aperture extreme ultraviolet microfield optic" J. Vac. Sci. Technol. B 23, 2003 (2005)

- [6] M. Born, and E. Wolf, "Principles of Optics", 6th Ed., Pergamon Press, New York, (1980).
- [7] F. X. Zach, C. Lin, and J. P. Kirk, "Aberration analysis using reconstructed aerial images of isolated contacts on attenuated phase-shift masks." SPIE 4346, 1362 (2001).
- [8] P. Dirksen, C. A. Juffermans, A. Casper; R. J. Pellens; M. Maenhoudt; P. Debisschop, "Novel aberration monitor for optical lithography" SPIE 3679, p. 77–86, Optical Microlithography XII. (1999).
- [9] P. Dirksen, J. Braat, A. J. E. M. Janssen, A. Leeuwestein, H. Kwinten, and D. Van Steenwinckel, "Determination of resist parameters using the extended Nijboer-Zernike theory" SPIE 5377, 150 (2004).
- [10] M. Mitchell "An introduction to genetic algorithms". MIT Press, (1998)



## Figure Captions

**Fig 1.** AIT zoneplate lens layout. All the measurements and the simulations described here, refer to an off-axis zoneplate lens with a numerical aperture of 0.0875, a focal length of 750  $\mu\text{m}$  and a working angle of 6 degrees.

**Fig 2.** A shows the local wavefront error and B shows the Strehl ratio over the field of view, for the AIT in perfect alignment conditions.

**Fig 3.** Local wavefront error distribution for the AIT in perfect alignment conditions without the defocus term contribution.

**Fig 4.** Unit cell samples for the aberrations test patterns. A: Simple square. B: Nested square. C: Symbol. D. Lines.

**Fig 5.** The merit function's behavior shows the aberration sensitivity of each test pattern through focus. For each pattern, the curves represent the calculated RMS difference between ideal and wavefront-aberrated images at different focal positions. The upper plot shows the case of 0.2 waves RMS of  $0^\circ$  astigmatism (Z4) and the lower plot shows the case of 0.05 waves RMS of X coma (Z6).

**Fig 6.** Reconstruction of a through focus series with the symbol pattern (C). We show here only one third of the image in the series that is actually made of thirteen images with evenly spaced focal planes. The upper panel shows the real images collected with the AIT and the lower panel shows the reconstruction.

**Fig 7.** The plots show the estimated value for the Zernike coefficients Z4 to Z7 in the middle of the field of view. The upper plot shows the values obtained using the symbol pattern (C) and lower plot shows the value obtained using the nested square pattern (B).

**Table 1.** Expected values of the main AIT aberrations expressed in terms of Zernike fringes polynomials. These values, calculated using a raytracing model of the AIT, are the maximum values for each component of the wavefront error when the system is in perfect alignment. For a system in a generic alignment state will be possible to have aberration values that exceed the ones shown here.

Aberration	FRINGE []	RMS []
Z3 Defocus	0.5307	0.3064
Z4 Astigmatism 0°	0.4837	0.1975
Z5 Astigmatism 45°	0.5341	0.2180
Z6X Coma	0.1274	0.0450
Z7Y Coma	0.1224	0.0433
Z8 Spherical	0.0015	0.0007

**Figure 1**

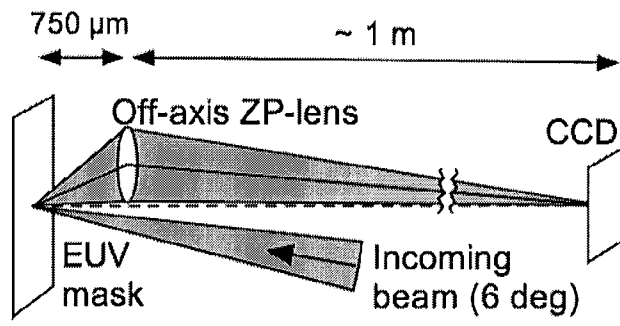


Figure 2

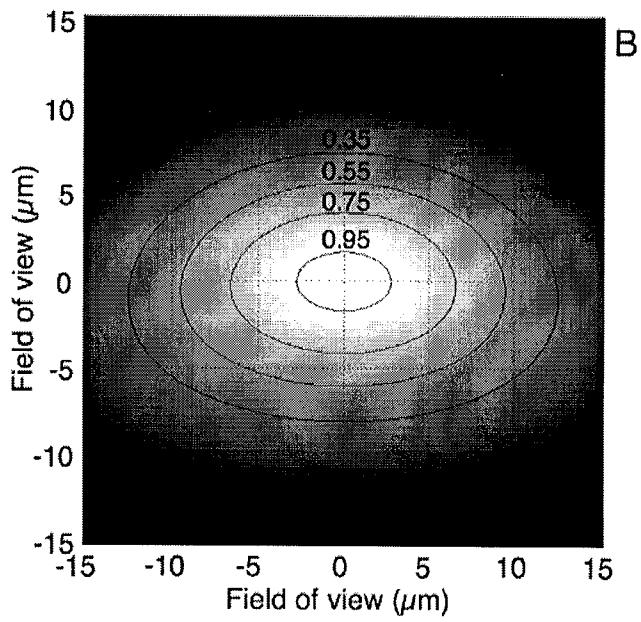
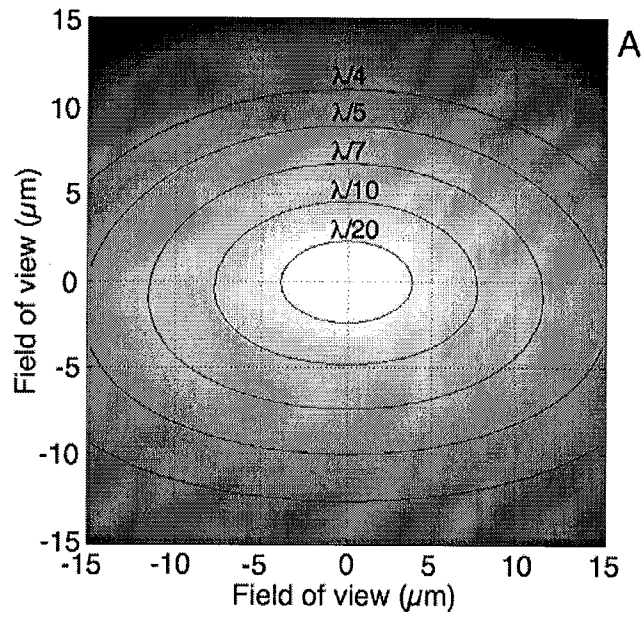


Figure 3

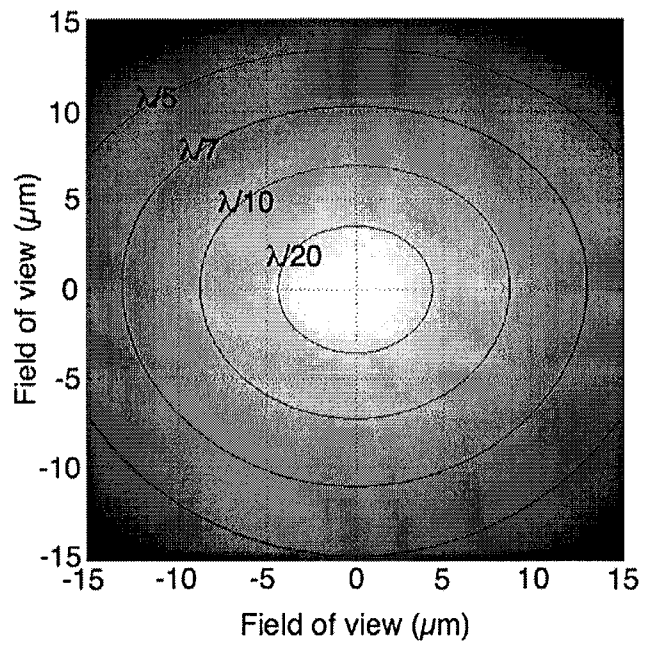
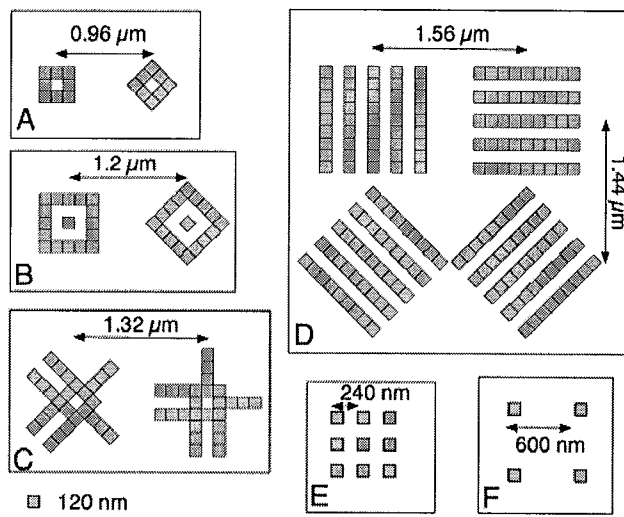
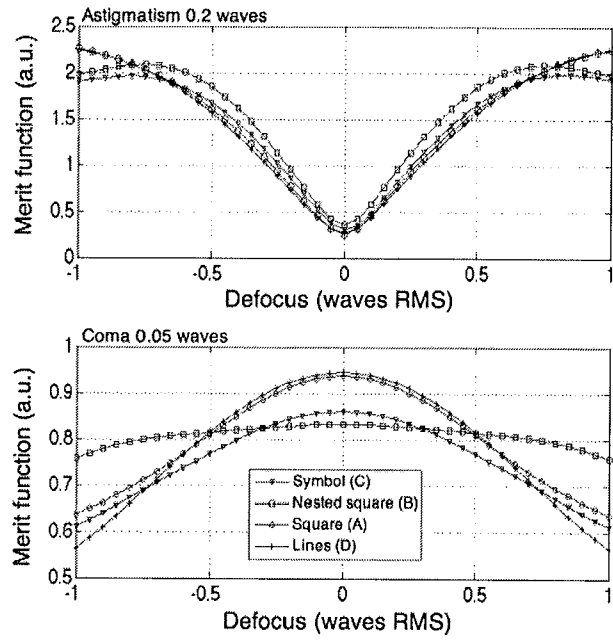


Figure 4



**Figure 5**



**Figure 6.**

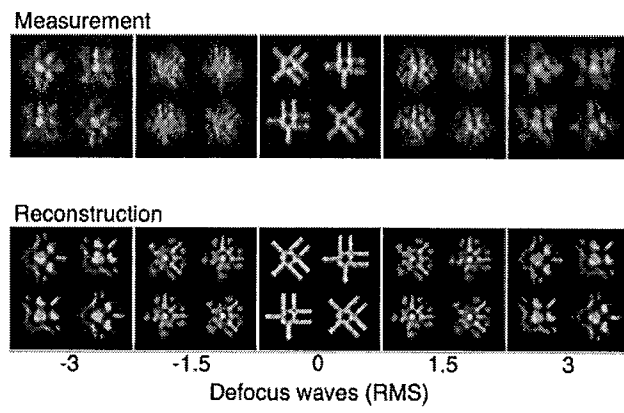




**Figure 7**

